Matter

Article

Adaptive nanofluidic ion sieving via voltage-induced sub-nanometer channel plasticity in MXene membranes

Graphical abstract

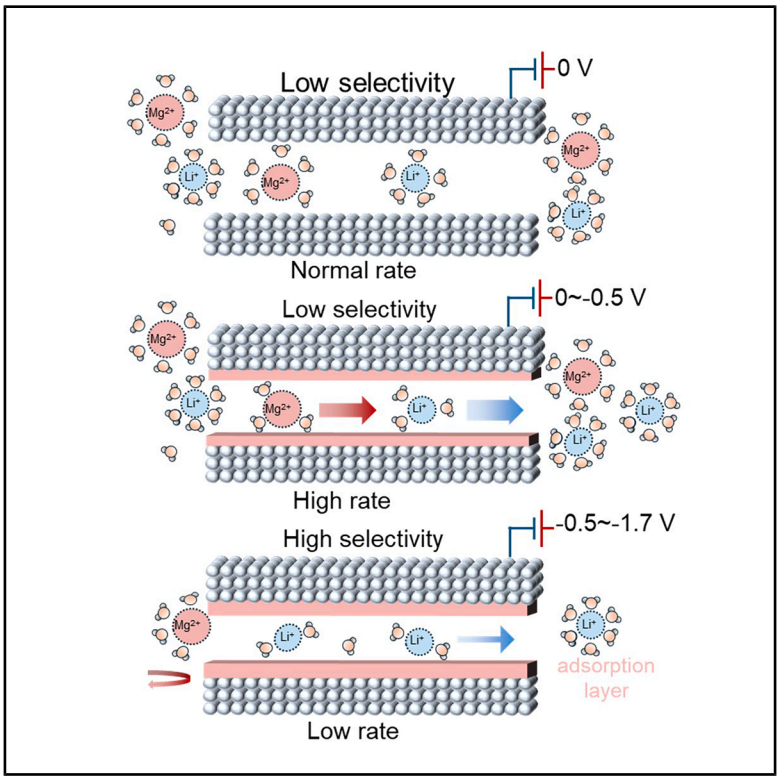

Highlights

- Voltage drives reversible channel shrinkage from 7.2 to 5.2 Å
- Dynamic structural gating enables mono/divalent ion discrimination
- Li^+/Mg^{2+} selectivity rises to 58.7 in real salt-lake brine
- Adaptive MXene membranes remain stable over 70 h of operation

Authors

Fuhao Yao, Engui Wang, Shixian Xin, ..., Tianqi Zhang, Zhiyong Tang, Jinlei Yang

Correspondence

yangjinlei@ucas.ac.cn

In brief

Most membranes separate ions via fixed channels, which limits the precision with which they can distinguish similar ionic species. Here, voltage induces the shrinkage of MXene membrane channels, creating an adaptive pathway that allows lithium ions to pass while blocking magnesium ions. This work introduces the concept of electrically programmed channel plasticity for constructing smarter separation membranes, with applications in lithium recovery, water treatment, and other ion-selective technologies.

Improvement
Enhanced performance with innovative design or material control

Yao et al., 2026, Matter 9, 102854
September 2, 2026
https://doi.org/10.1016/j.matt.2026.102854

CellPress

Please cite this article in press as: Yao et al., Adaptive nanofluidic ion sieving via voltage-induced sub-nanometer channel plasticity in MXene membranes, Matter (2026), https://doi.org/10.1016/j.matt.2026.102854

Matter

CellPress

Article

Adaptive nanofluidic ion sieving via voltage-induced sub-nanometer channel plasticity in MXene membranes

Fuhao Yao,[1] Engui Wang,[1] Shixian Xin,[1] Linghao Liu,[1] Han Xie,[1] Hao Wang,[1] Yan Wang,[1] Han Ouyang,[1] Tianqi Zhang,[2] Zhiyong Tang,[2] and Jinlei Yang[1,3,*]

[1]University of Chinese Academy of Sciences, Beijing, China
[2]National Centre for Nanoscience and Technology, Beijing, China
[3]Lead contact
*Correspondence: yangjinlei@ucas.ac.cn
https://doi.org/10.1016/j.matt.2026.102854

PROGRESS AND POTENTIAL This work addresses a central limitation in membrane-based ion separations: conventional nanochannels are structurally static, so improving selectivity often comes at the expense of permeability. We show that a conductive $Ti_3C_2T_x$ MXene/bacterial cellulose membrane can instead function as an adaptive nanofluidic sieve, in which an applied voltage actively reconfigures the transport channel during operation. The key advance is a reversible voltage-induced contraction of the interlayer spacing from 7.2 to 5.2 Å, coupled with enhanced interfacial charge and ion-specific adsorption. This dynamic structural gating enables the membrane to move from a relatively open transport state to a highly selective sieving state, allowing monovalent ions to continue passing while strongly suppressing divalent ions.

As a result, the membrane achieves nearly complete mono/divalent ion discrimination under negative bias, while maintaining substantial Li^+ transport. The effect is robust over repeated switching cycles and remains stable during 70 h of continuous operation. Importantly, the concept also translates to realistic brine conditions, where Li^+/Mg^{2+} selectivity is greatly improved. Beyond the immediate relevance to lithium extraction, this study establishes a broader design principle for responsive membranes: selectivity can be programmed not only by fixed chemistry or pore size but also by stimulus-driven channel plasticity. This opens a path toward intelligent ion-separation systems for resource recovery, water treatment, and electrochemical separations.

SUMMARY

Selective Li^+/Mg^{2+} separation remains challenging because static membrane nanochannels are constrained by the permeability-selectivity trade-off. Here, we report a conductive $Ti_3C_2T_x$ MXene/bacterial cellulose membrane that enables voltage-gated ion sieving through reversible nanochannel contraction. Applying a membrane potential induces interfacial charge enrichment and ion-specific adsorption, driving dynamic interlayer shrinkage from 7.2 to 5.2 Å and creating an adaptive steric barrier for divalent ions. At −1.7 V, the membrane nearly completely blocks Mg^{2+} and Ca^{2+} while maintaining substantial monovalent fluxes (K^+: 60.6 and Li^+: 25.9 mmol m^{-2} h^{-1} at 0.1 M). The membrane remains stable for 70 h and shows reversible performance over repeated voltage cycles. In real salt-lake brine, Li^+/Mg^{2+} selectivity increases from 0.2 to 58.7. This work establishes dynamic structural gating as a strategy for programmable nanofluidic ion separation.

INTRODUCTION

Lithium ions (Li^+) are pivotal strategic resources for emerging energy technologies, with global demand surging due to the rapid expansion of electric vehicles and energy storage systems.[1,2] Efficient extraction of Li^+ from salt-lake brines is essential to alleviate supply constraints and promote sustainable development.[3–5] Compared to conventional processes such as precipitation, adsorption, and solvent extraction, membrane separation presents an attractive alternative owing to its low energy consumption, operational simplicity, and environmental compatibility.[6–9] However, practical application remains challenging

Please cite this article in press as: Yao et al., Adaptive nanofluidic ion sieving via voltage-induced sub-nanometer channel plasticity in MXene membranes, Matter (2026), https://doi.org/10.1016/j.matt.2026.102854

because abundant Mg^{2+} competes with Li^{+} during transport. Fundamentally, the similar hydrated radii of these ions (Li^{+}: 3.82 Å; Mg^{2+}: 4.28 Å) and the inherent permeability-selectivity trade-off in static solution-diffusion nonporous membranes collectively limit extraction efficiency.[10–12]

In nature, biological ion channels (e.g., KcsA) achieve extraordinary selectivity through adaptive conformational changes, responding dynamically to external stimuli.[13] In contrast, most artificial membranes remain "static" architectures with fixed pore sizes,[14–16] struggling to break the permeability-selectivity trade-off. To bridge this gap, nanofluidic transistors inspired by these biological gates have been developed to actively modulate ion transport via gate-controlled surface charges.[17–20] The direction and rate of ion transport within nanochannels can be finely and dynamically tuned—a process collectively governed by the nano-confinement, surface properties, and gate voltage polarity.[21–25] Recent advances in two-dimensional (2D) laminar membranes—such as graphene and transition metal carbides (MXenes)—showcase exceptional potential for selective mass transport.[26–33] In these laminar membranes, selectivity primarily arises from precise size exclusion within the nanochannels formed between stacked nanosheets.[34–36] This molecular sieving effect, augmented by nanoconfined electrostatic interactions, accounts for their superior performance in balancing selectivity with permeability.[12,37–39] However, state-of-the-art strategies predominantly focus on tuning surface charge density or exploiting ion-charge interactions within structurally rigid frameworks. For instance, recent studies have utilized inorganic pillars[29] or polymer confinement[25] to stabilize the interlayer spacing, thereby isolating electrostatic gating effects. While effective for flux modulation, these "static" designs inherently sacrifice the dynamic structural plasticity—voltage-induced reversible channel variation—required for high-precision, angstrom-scale molecular sieving.

Here, we report a distinct physical phenomenon that addresses this challenge: a voltage-induced, large-scale interlayer contraction in $Ti_3C_2T_X$ MXene/bacterial cellulose (BC) composite membranes. Unlike previous works relying solely on electrostatic shielding, we demonstrate a "dynamic structural gating" mechanism where an applied gate potential concurrently enhances interfacial charge and drives a real-time, reversible contraction of the nanochannels from 7.2 to 5.2 Å. This dual-parameter control—encompassing both electrochemical potential and geometric plasticity—enables angstrom-precise tuning of the channel geometry. Driven by ion-specific adsorption, this behavior yields exceptional steric-hindrance-based selectivity that mirrors the adaptive nature of biological systems.

RESULTS

Fabrication and structural architecture

MXene/BC composite clusters were prepared through spontaneous adsorption between $Ti_3C_2T_X$ nanosheets and bacterial cellulose (BC), as illustrated in Figure 1A. BC serves as a naturally renewable and chemically stable biomaterial that synergizes with MXene to improve overall performance. Through hydrogen bonding among surface moieties (–OH, F on $Ti_3C_2T_X$ and –OH on BC), it prevents nanosheet stacking and enhances interfacial adhesion while providing abundant active sites. This enables self-assembly into stable precursors for membrane fabrication.[40] A series of freestanding laminar membranes were then fabricated via vacuum filtration by a fixed mass of $Ti_3C_2T_X$ (50 mg) with varying amounts of BC (0, 2.5, 5, and 7.5 mg), yielding samples denoted as M-0 (pristine MXene), M-5, M-10, and M-15 (corresponding to 0, 5, 10, and 15 wt % BC). The mechanical robustness of the composites is attributed to BC-introduced interfacial hydrogen bonding, which enhances interlayer adhesion and overall stability (Figures 1B and S1). Surface scanning electron microscopy (SEM) images showed that all membranes maintain the characteristic wrinkled morphology of MXene, with uniformly distributed BC imparting slight surface roughness without causing agglomeration (Figure 1B). Cross-sectional analysis revealed a highly oriented laminar stacking structure, with membrane thickness increasing from 17.4 μm (M-0) to 23.2 μm (M-15) as BC content rises (Figure 1C). X-ray diffraction (XRD) patterns for all components exhibited distinct diffraction features (Figure S2). The effective interlayer spacing, defined as the total interlayer height subtracting the thickness of a single $Ti_3C_2T_X$ nanosheet,[39] was quantified. The M-0 membrane exhibited significant swelling, expanding from 3.3 Å (dry state) to 6.1 Å (wet state). In contrast, BC-doped membranes showed suppressed swelling; the dry-state effective interlayer spacings of 4.4 Å, 5.3 Å, and 5.6 Å for M-5, M-10, and M-15 increased only to 6.5 Å, 7.0 Å, and 7.8 Å in the wet state, respectively (Figures 1D and 1E). This confirms the role of BC-MXene hydrogen bonding in inhibiting interlayer swelling and stabilizing the nanochannel structure. Furthermore, the conductivity of the membranes was further evaluated (Figure 1F). All membranes retained high conductivity, with values of 1,916 S/cm (M-0); 1,739 S/cm (M-5); 1,605 S/cm (M-10); and 1,492 S/cm (M-15), which is essential for rapid response to external voltage stimuli in subsequent ion transport studies.

Voltage-gated ion transport

To investigate the voltage-gated ion transport behavior in MXene/BC hybrid membranes, we constructed an H-type diffusion cell as a nanofluidic testing platform (Figure 2A). The permeation of ions was monitored using inductively coupled plasma optical emission spectrometry (ICP-OES). Ion transport was driven by concentration gradient and electric field, with a 0.1 M mixed chloride salt solution (K^{+}, Li^{+}, Ca^{2+}, Mg^{2+}; 1:1:1:1 molar ratio) on the feed side and deionized (DI) water on the permeate side. We first evaluated the intrinsic membrane selectivity in the absence of an external voltage. As shown in Figure 2B (left), the cumulative permeation of all four ions increased linearly over time, but with distinct rates. Typically, the M-5 membrane exhibited a K^{+} permeation rate of 198.5 mmol m^{-2} h^{-1}, while the rates for Li^{+}, Ca^{2+}, and Mg^{2+} were all below 100.0 mmol m^{-2} h^{-1}. A similar trend was observed for M-10 and M-15 (Figure S3). In comparison, the pristine M-0 membrane exhibited permeation rates that were nearly 2-fold lower for all ions (Figure 2B, right). The enhancement of the composite membranes can be attributed to their enlarged interlayer spacing after BC doping, as corroborated by Figure 1E, and their improved hydrophilicity, supported by contact angle measurements (Figure S4).

Please cite this article in press as: Yao et al., Adaptive nanofluidic ion sieving via voltage-induced sub-nanometer channel plasticity in MXene membranes, Matter (2026), https://doi.org/10.1016/j.matt.2026.102854

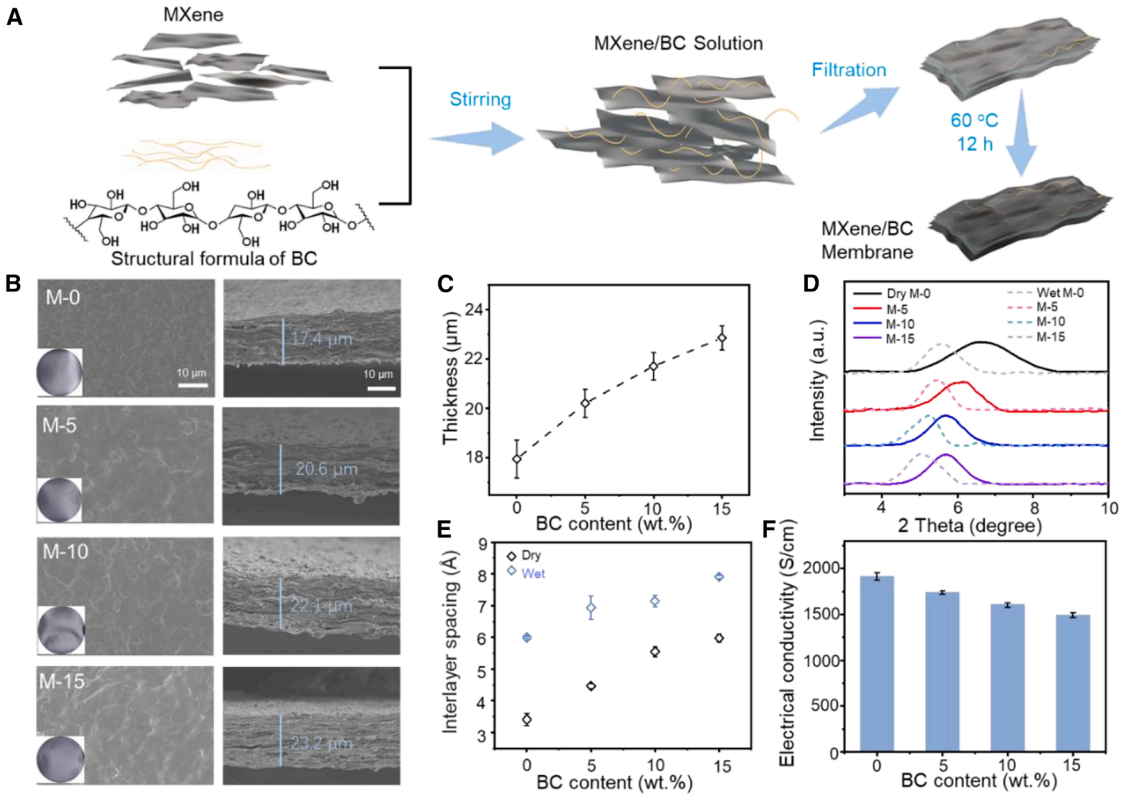

Figure 1. Fabrication and structural characterization of adaptive MXene/BC composite membrane

(A) Schematic illustration of the fabrication process of the self-assembly of $Ti_3C_2T_X$ nanosheets and BC nanofibers into a resilient framework.

(B) Surface and cross-sectional SEM images, along with digital photographs, of the membranes with varying BC contents: M-0 (0 wt %), M-5 (5 wt %), M-10 (10 wt %), M-15 (15 wt %).

(C) Membrane thickness as a function of BC content.

(D and E) Comparison of XRD patterns and interlayer spacings in dry and wet states. Wet states represent the immersion in a mixed salt solution including KCl, LiCl, $CaCl_2$, and $MgCl_2$ (0.1 M).

(F) Electrical conductivity of the membranes with different BC contents.

Error bars represent the SD with three parallel experiments.

We next evaluated the effect of membrane potential on ion sieving performance. To ensure accurate control of the electrical potential across the membrane, the applied voltage was calibrated against the actual membrane potential via electrochemical impedance measurements (Figure S5). Upon applied gate voltages, ion permeation showed pronounced modulation under negative membrane potentials but responded weakly to positive potentials (Figure S6), which is primarily due to the high intrinsic negative surface charge density of the pristine membrane (zeta potential −40 mV; Figure S7).[25,41] Specifically, the M-5 membrane exhibited a distinct two-stage "enhancement-inhibition" behavior in voltage-gated ion permeation (Figure 2C). When the membrane potential was tuned from 0 to −0.5 V, the permeation rates of all ions increased. At −1.3 V, the permeation rates of K^+, Li^+, and Mg^{2+} dropped to 118.7, 47.4, and 1.1 mmol m^{-2} h^{-1}, respectively, yielding high K^+/Mg^{2+} and Li^+/Mg^{2+} selectivities of 231.1 and 74.6 (Figures 2E and 2F). Furthermore, Ca^{2+} and Mg^{2+} became nearly undetectable in the permeate side (<0.01 ppm) at −1.7 V, while K^+ and Li^+ maintained fluxes of 60.6 and 25.9 mmol m^{-2} h^{-1}, achieving nearly complete mono-/divalent ion separation. To better visualize the voltage-gated transport behavior, we normalized the permeation rates of the four ions to their corresponding values at 0 V (Figures 2D and S8). This pronounced valence-dependent regulation confirms that the membrane can effectively distinguish and regulate the transport of ions with different valences through voltage modulation. Cyclic voltammetry confirms that the applied membrane potential of −1.7 V exceeds the theoretical water electrolysis window, inducing water splitting (Figure S9). To evaluate the impact of these electrochemical reactions on the nanochannels, we systematically monitored the pH evolution. The local pH variations proved to be relatively mild, with the feed and permeate solutions stabilizing at approximately 4.0 and 7.8, respectively (Figures S10A and S10B). Furthermore, the membrane exhibits highly consistent Li^+/Mg^{2+} separation performance across a remarkably broad pH range from 3.0 to 9.5 (Figure S10C). Crucially, alongside this stable selectivity, a notable and continuous monovalent ion flux is well maintained during operation. These results demonstrate that localized pH fluctuations and gas evolution have a negligible impact on the membrane's structural integrity and ion sieving efficiency.

Please cite this article in press as: Yao et al., Adaptive nanofluidic ion sieving via voltage-induced sub-nanometer channel plasticity in MXene membranes, Matter (2026), https://doi.org/10.1016/j.matt.2026.102854

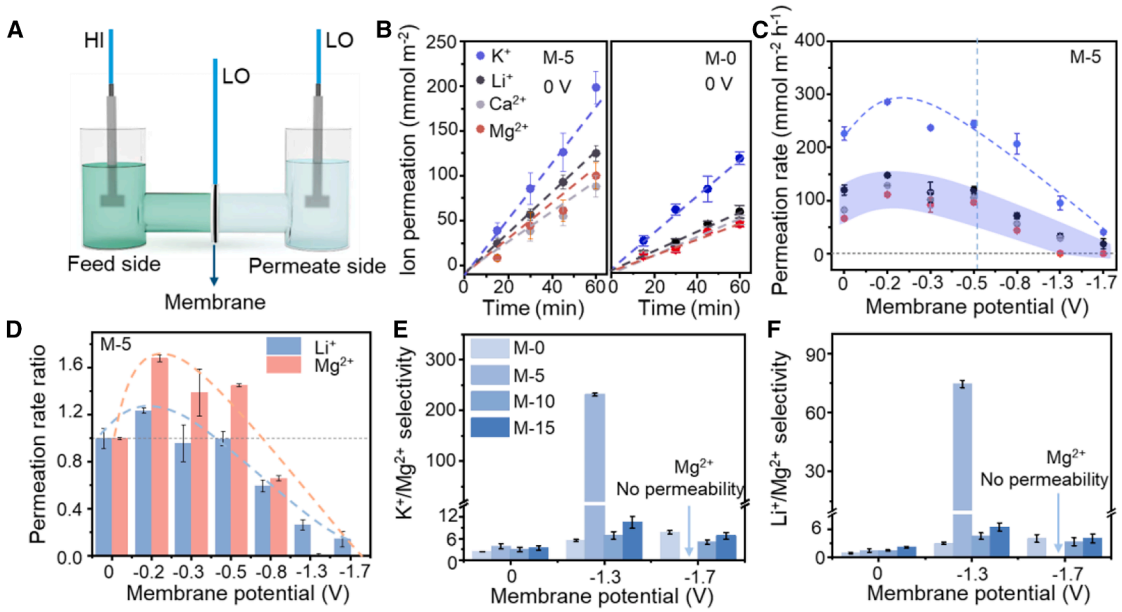

Figure 2. Voltage-gated ion transport and selective molecular sieving

(A) Schematic of the nanofluidic platform configured for active potential control.

(B) Comparison of intrinsic ion permeation kinetics between M-0 and M-5, highlighting the BC-induced flux enhancement.

(C and D) Voltage-dependent transport profiles illustrating the enhancement-to-inhibition transition measured over 15 min. The normalized ratios reveal a distinct valence-dependent regulation.

(E and F) Exceptional K^+/Mg^{2+} and Li^+/Mg^{2+} selectivity of MXene/BC membranes (M-0, M-5, M-10, and M-15) under negative membrane potentials, showing the transition from a non-selective channel to a high-precision ionic sieve.

Error bars represent the SD with three parallel experiments.

A distinctive characteristic is the uniquely high ion selectivity of the M-5 membrane under an applied negative voltage. In contrast, the other membranes (M-0, M-10, and M-15) exhibit ineffective ion separation performance (Figures 2E, 2F, and S11). For pristine M-0 membrane, its susceptibility to swelling and structural instability in solution probably prevents stable voltage-gated regulation,[38] leading to performance degradation. Furthermore, the diminished separation performance of M-10 and M-15 is presumably attributed to the structural heterogeneity induced by excessive BC content. While voltage modulation still triggers lattice contraction in the MXene domains (as evidenced by XRD), the elevated BC loading tends to cause localized agglomeration and disrupt the continuous laminar stacking.[42] These disruptions likely create non-selective interfacial voids or defects that act as leakage pathways. Consequently, even if the bulk interlayer spacing contracts, ions can bypass the sieving channels through these defects, weakening the overall 2D nanoconfinement effect essential for high-precision separation. These findings establish that an appropriate BC (5 wt %) presents an optimal balance, ensuring sufficient structural integrity to support interlayer contraction for ion transport under voltage-gated modulation. Thickness-dependent evaluations demonstrate that the voltage-gating mechanism is intrinsic to the MXene laminates and functions robustly independent of thickness, seamlessly trading higher permeability in thinner membranes for enhanced selectivity in thicker ones (Figure S12). Furthermore, we also investigate the effect of concentration variation on voltage-regulated transport behavior and found that the membrane still effectively retained divalent ions (Ca^{2+}, Mg^{2+}) and also exhibited the "enhancement-inhibition" response to membrane potential (Figure S13).

Mechanism of lattice plasticity

To elucidate the mechanism of voltage-regulated ion separation, we first evaluated the membrane surface charge density (σ) as a function of the applied voltage. The MXene/BC membranes exhibit a negative zeta potential (Figure S7) due to deprotonation of –OH groups.[41] As shown in Figures 3A and S14, σ shows a clear voltage dependence, with an increment of approximately -35 mC m^{-2} at -1.7 V from its initial value at 0 V. This enhancement in negative surface charge strengthens electrostatic interactions between cations and the membrane. To isolate the direct electrophoretic contribution of the applied electric field, control experiments were conducted using a pure BC membrane (Figure S15). Unlike the MXene composite, the pure BC membrane exhibited a monotonic increase in ion flux without the characteristic voltage-gating behavior. This confirms that the dominant driving force is indeed the voltage-enhanced surface charge density of the MXene membrane, rather than the electric field. Another major regulatory mechanism is the steric hindrance effect, which arises from ion-adsorption-induced modulation of the interlayer spacing (d). In addition to cation-π interactions,[43] a clear rise in cation adsorption was observed with increasingly negative membrane potentials (Figure 3B and Table S2), quantified using an immersion-desorption approach (Figure S16). Typically, the adsorption behavior under negative

Please cite this article in press as: Yao et al., Adaptive nanofluidic ion sieving via voltage-induced sub-nanometer channel plasticity in MXene membranes, Matter (2026), https://doi.org/10.1016/j.matt.2026.102854

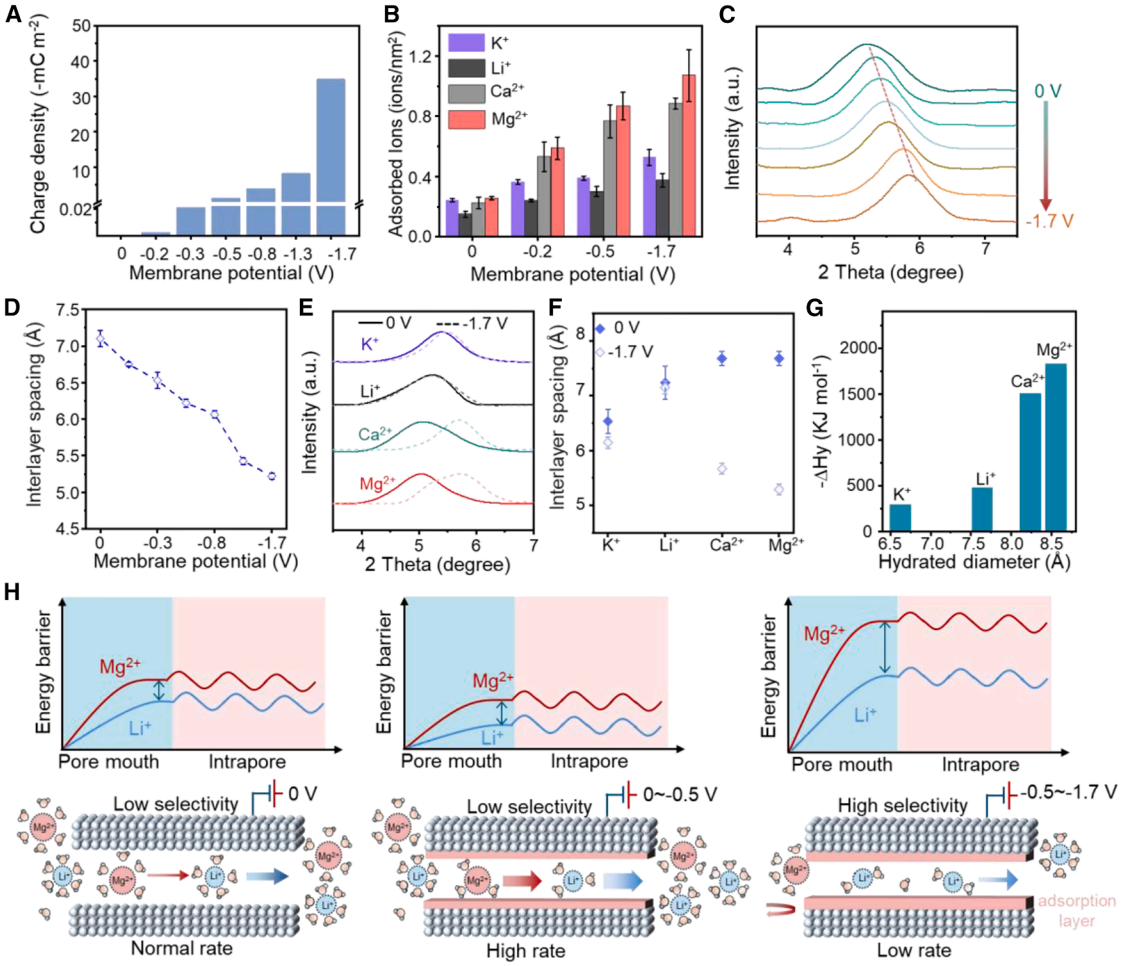

Figure 3. Mechanism of ion-adsorption-driven lattice plasticity

(A and B) Correlation between gate-induced surface charge density and valence-dependent cation adsorption, providing the electrochemical driving force for structural change.

(C and D) XRD profiles of continuous membrane interlayer shrinkage under applied potentials. The progressive peak shift directly quantifies the dynamic lattice plasticity from 7.2 to 5.2 Å.

(E and F) Comparative XRD analysis of wet membranes under single-salt environments, illustrating the role of divalent ions in triggering pronounced channel narrowing.

(G) Hydration energy and hydrated diameter of each ion species.

(H) Theoretical energy-barrier model illustrating the synergy between pore-mouth partitioning and steric-hindered intrapore diffusion during the structural transition from "open" to "sieving" states.

Error bars represent the SD with three parallel experiments.

potentials is valence-dependent: divalent ions (Ca^{2+} and Mg^{2+}) exhibit a substantial rise in adsorption density, from below ~0.30 ions nm^{-2} at 0 V to ~0.88 and ~1.07 ions nm^{-2} at −1.7 V, respectively, while the adsorption of monovalent ions increases moderately, remaining below ~0.52 ions nm^{-2}. Consequently, the voltage-regulated ion adsorption significantly influences the interlayer spacing of the membrane. *Ex situ* XRD analysis was employed to systematically elucidate the synergistic regulation of *d* by different ion species and membrane potentials (experimental section). As shown in the diffraction patterns (Figure 3C), the progressive shift of XRD diffraction peaks toward higher 2θ angles with increasingly negative potentials (0 V to −1.7 V) directly indicates a continuous shrinkage of *d*. Quantitatively, the spacing decreases from 7.2 Å at 0 V to 5.2 Å at −1.7 V (Figure 3D). Further analysis of the diffraction profiles and derived d values for K^+, Li^+, Ca^{2+}, and Mg^{2+} reveals distinct valence-dependent behavior (Figures 3E and 3F). Under −1.7 V, divalent ions promote more pronounced channel narrowing compared to monovalent ions, playing a dominant role in the voltage-induced confinement effect. Basically, the entrance of ions into nanoconfined spaces requires overcoming the hydration energy barrier while balancing interactions with the membrane surface.[44–46] The applied membrane potential alters this balance by enhancing the electrostatic forces, not only promoting ion entry but also preferentially facilitating the penetration of larger divalent ions despite their higher hydration energy

Please cite this article in press as: Yao et al., Adaptive nanofluidic ion sieving via voltage-induced sub-nanometer channel plasticity in MXene membranes, Matter (2026), https://doi.org/10.1016/j.matt.2026.102854

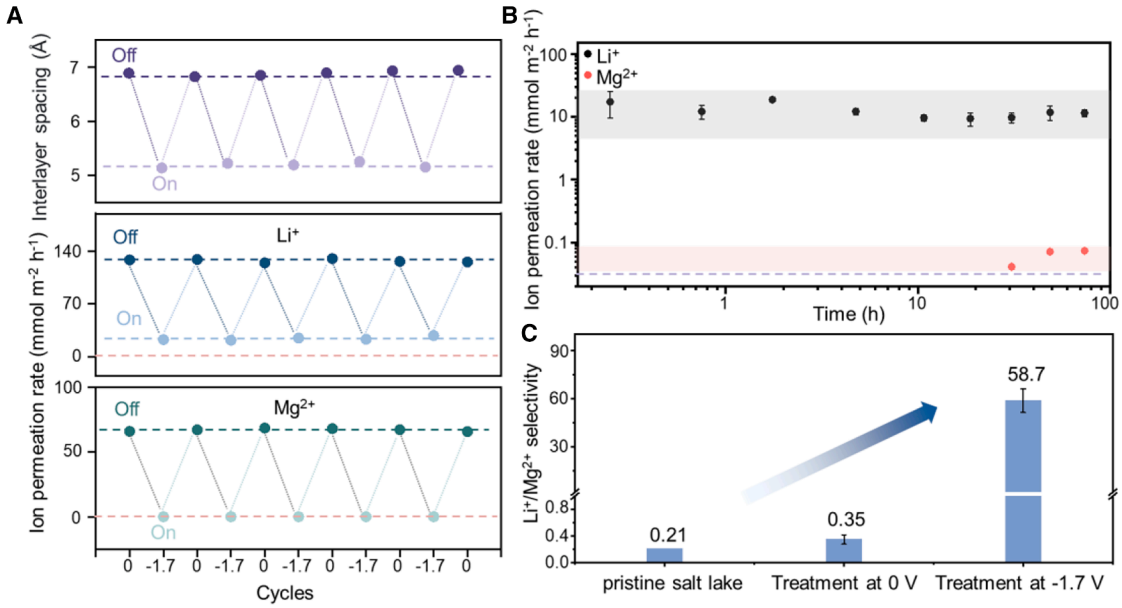

Figure 4. Robustness and practicality of the adaptive nanofluidic sieve

(A) Cyclic reversibility of both the interlayer lattice spacing and Li^+/Mg^{2+} separation performance (on: −1.7 V, off: 0 V).

(B) Long-term operational stability over 70 h, showing the durability of the electro-structural coupling under constant polarization (−1.7 V).

(C) High-efficiency lithium extraction from real salt-lake brines.

Error bars represent the SD with three parallel experiments.

(Figures 3G, 2C, and 2D), thereby introducing an additional dimension for precise ionic control.

Selective ion transport across the membrane is mainly governed by two sequential processes: pore mouth partitioning (regulated by hydration energy barriers) and intrapore diffusion (modulated by steric hindrance).[45,47] Both are dynamically controlled by voltage-induced changes in membrane surface charge and interlayer spacing (Figure 3H). At 0 V, K^+ and Li^+ show higher permeability than Ca^{2+} and Mg^{2+} (Figure 2B), attributable to their diffusion rate and hydration energy priority (Figure 3G and Table S1), which facilitates pore mouth partitioning and enables rapid intrapore diffusion. As the applied voltage increases to −0.5 V, σ increases to −1.2 mC m^{-2}, leading to an enhanced permeance especially for high-valence cations, despite the interlayer spacing contracts from 7.2 Å to 6.2 Å (Figure 3C). When the voltage further increases from −0.5 V to −1.7 V, permeation rates continuously decline. In this regime, σ surges to −35 mC·m^{-2} (Figure 3A), strongly promoting electrostatic adsorption of divalent ions and shrinking the interlayer spacing to 5.2 Å, only 0.7 Å larger than the dry-state spacing (Figure 3D). The narrowed channels impose severe steric restrictions on intrapore diffusion. Monovalent ions surmount the increased barriers to traverse the constricted pathways, while divalent ions are effectively retained through a synergistic strong electrostatic adsorption and steric hindrance, leading to nearly complete rejection.

Stability and practicality

We next investigated the stability and practicality performance of the MXene/BC composite membrane on voltage-gated lithium extraction. The reversibility and stability of voltage-gated ion transport in the M-5 membrane were evaluated by alternating the membrane potential between 0 and −1.7 V, combined with XRD characterization and ion flux measurements. Over five consecutive voltage-switching cycles, the interlayer spacing was reproducibly controlled via voltage regulation, and the M-5 membrane maintained nearly-complete Mg^{2+} rejection after these on-off cycles (Figure 4A). These results confirm the excellent reversible recyclability of both the voltage-regulated nanochannel structure and the resulting ion separation performance.

To evaluate the membrane performance under practical conditions, the M-5 membrane was subjected to a 70-h ion transport test under a constant applied voltage of −1.7 V (Figure 4B). Throughout the first 30 h, no Mg^{2+} was detected on the permeate side. Trace amounts of Mg^{2+} began to appear thereafter, with flux gradually increasing to only 0.04 mmol m^{-2} h^{-1} by the end of the test. Post-test SEM and XRD confirm this trace leakage is not from structural damage, as the membrane retains its delamination-free layered structure and stable ~7.2 Å interlayer spacing (Figure S17). In contrast, Li^+ permeation remained stable throughout entire duration. These results confirm that the M-5 membrane retains excellent structural and functional stability during long-term voltage-regulated operation. More impressively, in dealing with real Qaidam salt lake brine, Li^+/Mg^{2+} selectivity was dramatically enhanced from 0.2 to 58.7 (Figures 4C, S18, and S19), demonstrating efficient realistic salt lake lithium extraction.

DISCUSSION

In summary, we developed a conductive $Ti_3C_2T_X$ MXene/BC composite membrane that significantly enhances the Li^+/Mg^{2+}

Please cite this article in press as: Yao et al., Adaptive nanofluidic ion sieving via voltage-induced sub-nanometer channel plasticity in MXene membranes, Matter (2026), https://doi.org/10.1016/j.matt.2026.102854

separation through voltage-induced dynamic interlayer regulation. By leveraging the synergy between tunable surface charge and structural plasticity, the membrane transitions from a high-permeability state at low potentials to a high-precision sieving state at high potentials. This transition involves a reversible shrinkage of the nanochannels to 5.2 Å, effectively blocking divalent ions while maintaining efficient monovalent transport. The membrane demonstrates exceptional stability over 70 h of operation and maintains consistent performance across repeated voltage cycles. In real-world salt-lake brines, the Li^+/Mg^{2+} selectivity was enhanced from 0.2 to 58.7, proving its practical utility. Beyond lithium extraction, this work establishes a new paradigm for adaptive nanofluidic separation, offering valuable insights for the design of programmable, intelligent membranes for water purification and advanced ionic devices.

METHODS

Preparation of MXene nanosheets

The $Ti_3C_2T_X$ MXene nanosheets were synthesized by selectively etching the aluminum layer from the Ti_3AlC_2 MAX phase. In a typical procedure, 5 mL of DI water was mixed with 15 mL of concentrated hydrochloric acid (36%–38%), after which 1 g of lithium fluoride (LiF) and 1 g of Ti_3AlC_2 powder were added to the mixture. The reaction was carried out under continuous stirring at 40°C for 24 h. The resulting suspension was then diluted with 15 mL of DI water and centrifuged at 3,500 rpm for 3 min. The supernatant was discarded, and the sediment was rinsed repeatedly with DI water and centrifuged until the supernatant reached a pH of approximately 6.0. The collected precipitate was redispersed in DI water and ultrasonicated in an ice bath for 1 h. Finally, the dispersion is centrifuged at 3,500 rpm for 60 min to isolate the supernatant containing delaminated single-layer $Ti_3C_2T_X$ nanosheets.

Characterization

Elemental composition of the ion permeation samples is determined by inductively coupled plasma optical emission spectrometry (ICP-OES, Thermo Fisher Scientific iCAP Q, USA). Surface morphology and microstructure were examined via scanning electron microscopy (SEM, Hitachi Regulus 8220, Japan). Crystalline structures were characterized by XRD (Bruker D8 VENTURE, Germany). Different BC-doped samples were characterized by contact angle goniometry (CAG, ramé-hart 210 Series, USA). Specific surface areas of the samples were measured using a physisorption analyzer (BET, Micromeritics TriStar II Plus Series, USA). The zeta potentials were analyzed using a zeta potential analyzer (Zetasizer Nano ZS, Malvern, UK). The electrical conductivities of membranes were tested using a multifunction digital four-probe tester (HPS2662, China).

Voltage-gated ion separation measurement

The tested membrane was mounted between two compartments of a diffusion cell. The feed compartment contained a 0.1 M equimolar mixed solution of KCl, LiCl, $CaCl_2$, and $MgCl_2$, while the permeate compartment was filled with DI water, establishing a constant concentration gradient across the membrane. A Keithley 2636B source meter operating in potentiostatic mode was used to apply voltage. Platinum electrodes were placed with the feed side connected to the high-potential terminal and the permeate side to the low-potential terminal.

Variable-voltage electrochemical characterization of MXene/BC membranes

Surface charge density under different membrane potentials was calculated using the equation:

$$Q = \frac{I \times t}{A_S}$$

where Q is charge density (mC m^{-2}), I is current (mA), t is time (s), and A_s is membrane surface area (m^2). Measurements were conducted in electrolyte solution with the membrane serving as the working electrode. The resulting current-time (I-t) curves and derived charge density reflect the electrochemical activity and charge storage behavior of the membrane under voltage, providing key indicators for evaluating its performance in voltage-gated ion separation.

Ion adsorption test of MXene/BC composite membranes

The MXene/BC composite membrane was immersed in a 0.1 M mixed salt solution (KCl, LiCl, $CaCl_2$, $MgCl_2$; 1:1:1:1 molar ratio) and subjected to a potential of −1.7 V for 15 min to facilitate ion adsorption. After polarization, the membrane was removed and gently rinsed with a small amount of DI water to remove loosely bound surface ions. The membrane was then transferred into DI water and soaked for 10 h to allow desorption of the adsorbed ions. After reaching equilibrium, the ion concentration in the aqueous phase was determined by ICP-OES, and the adsorption capacity of the membrane for each ion was calculated accordingly. Based on the total membrane thickness and the single-layer height, the number of layers was estimated, from which the total available surface area for ion adsorption was derived. Combined with the ICP-OES data, the number of adsorbed ions was calculated, allowing the determination of the number of adsorbed ions per square nanometer.

Characterization of dynamic structural reconfiguration

The crystal structure and interlayer dynamics were characterized by XRD. To quantify the voltage-induced lattice plasticity, XRD patterns were recorded under various polarization states. For *ex situ* structural analysis, the membrane was polarized at specific potentials in the mixed-salt electrolyte, followed by rapid characterization to capture the adsorption-induced lattice strain.

XRD data explicitly show that the contracted interlayer spacing securely persists even after the external field is removed (Figure 3). Crucially, XRD fundamentally probes long-range crystalline order. If the enriched ions merely remained in a disordered, free-flowing liquid phase at the interface, they could neither form a stable crystal structure nor induce a coherent shift in the Bragg diffraction. The persistent and well-defined shift of the characteristic diffraction peak strictly demonstrates that the ions are not in a liquid-phase state; rather, they are fixedly adsorbed and immobilized within the interlamellar space, establishing a highly ordered, solid-like intercalated structure.

Cyclic performance tests

Cyclic tests were conducted to evaluate the reversibility of both interlayer spacing and ion permeation. For interlayer spacing reversibility, XRD analysis was performed on the membrane before applying voltage, after being held at −1.7 V for 15 min, and again after soaking in DI water for 10 h. For ion permeation reversibility, the membrane was subjected to alternating 15-min intervals without voltage and with −1.7 V applied. Permeate samples were collected during each interval for ICP analysis, and the voltage-switching procedure was repeated over five consecutive cycles. To completely remove adsorbed ions between test cycles, both reservoirs were thoroughly rinsed and refilled with ultrapure water. Continuous I-V scans (sweeping from −1.5 V to +1.5 V for ∼20 cycles) were then applied to electrochemically drive residual ions out of the membrane interlayers. Following a final rinse, the system was considered ready for the subsequent cycle only when the water conductivity dropped to ∼1 μS/cm.

RESOURCE AVAILABILITY

Lead contact

Further information and requests for resources and reagents should be directed to and will be fulfilled by the lead contact, Jinlei Yang(yangjinlei@ucas.ac.cn).

Materials availability

The materials generated in this study are available from the corresponding author upon request.

Data and code availability

The data and code are available upon reasonable request.

ACKNOWLEDGMENTS

The authors acknowledge financial support from the National Natural Science Foundation of China (22305246 and 52573354, J.Y.) and Fundamental Research Funds for the Central Universities (J.Y.).

AUTHOR CONTRIBUTIONS

F.Y. and J.Y. designed the experiments and co-wrote the manuscript. E.W. assisted in material synthesis. S.X., L.L., H.X., H.W., Y.W., O.Y., T.Z., and Z.T. helped F.Y. with the analysis and interpretation of results. All authors contributed to the discussion and writing of the manuscript.

DECLARATION OF INTERESTS

The authors declare no competing interests.

SUPPLEMENTAL INFORMATION

Supplemental information can be found online at https://doi.org/10.1016/j.matt.2026.102854.

Received: January 7, 2026
Revised: March 11, 2026
Accepted: May 1, 2026

REFERENCES

1. Ningthoujam, J. (2017). The Growing Role of Minerals and Metals for a Low Carbon Future (World Bank Group).
2. Chen, X., Yang, M., Zheng, S., Temprano-Coleto, F., Dong, Q., Cheng, G., Yao, N., Stone, H.A., Hu, L., and Ren, Z.J. (2023). Spatially separated crystallization for selective lithium extraction from saline water. Nat. Water *1*, 808–817. https://doi.org/10.1038/s44221-023-00131-3.
3. Vera, M.L., Torres, W.R., Galli, C.I., Chagnes, A., and Flexer, V. (2023). Environmental impact of direct lithium extraction from brines. Nat. Rev. Earth Environ. *4*, 149–165. https://doi.org/10.1038/s43017-022-00387-5.
4. Stringfellow, W.T., and Dobson, P.F. (2021). Technology for the Recovery of Lithium from Geothermal Brines. Energies *14*, 6805. https://doi.org/10.3390/en14206805.
5. Yong, M., Tang, M., Sun, L., Xiong, F., Xie, L., Zeng, G., Ren, X., Wang, K., Cheng, Y., Li, Z., et al. (2024). Sustainable lithium extraction and magnesium hydroxide co-production from salt-lake brines. Nat. Sustain. *7*, 1662–1671. https://doi.org/10.1038/s41893-024-01435-2.
6. Tian, X., Ye, C., Zhang, L., Sugumar, M.K., Zhao, Y., McKeown, N.B., Margadonna, S., and Tan, R. (2025). Enhancing Membrane Materials for Efficient Li Recycling and Recovery. Adv. Mater. *37*, 2402335. https://doi.org/10.1002/adma.202402335.
7. Kim, S., Wang, H., and Lee, Y.M. (2019). 2D Nanosheets and Their Composite Membranes for Water, Gas, and Ion Separation. Angew. Chem. *58*, 17512–17527. https://doi.org/10.1002/anie.201814349.
8. Werber, J.R., Osuji, C.O., and Elimelech, M. (2016). Materials for next-generation desalination and water purification membranes. Nat. Rev. Mater. *1*, 16018. https://doi.org/10.1038/natrevmats.2016.18.
9. DuChanois, R.M., Porter, C.J., Violet, C., Verduzco, R., and Elimelech, M. (2021). Membrane Materials for Selective Ion Separations at the Water-Energy Nexus. Adv. Mater. *33*, e2101312. https://doi.org/10.1002/adma.202101312.
10. Park, H.B., Kamcev, J., Robeson, L.M., Elimelech, M., and Freeman, B.D. (2017). Maximizing the right stuff: The trade-off between membrane permeability and selectivity. Science *356*, eaab0530. https://doi.org/10.1126/science.aab0530.
11. Korros, W.J., and Zhang, C. (2017). Materials for next-generation molecularly selective synthetic membranes. Nat. Mater. *16*, 289–297. https://doi.org/10.1038/nmat4805.
12. Shen, J., Liu, G., Han, Y., and Jin, W. (2021). Artificial channels for confined mass transport at the sub-nanometre scale. Nat. Rev. Mater. *6*, 294–312. https://doi.org/10.1038/s41578-020-00268-7.
13. Doyle, D.A., Morais Cabral, J., Pfuetzner, R.A., Kuo, A., Gulbis, J.M., Cohen, S.L., Chait, B.T., and MacKinnon, R. (1998). The structure of the potassium channel: molecular basis of K^+ conduction and selectivity. Science *280*, 69–77. https://doi.org/10.1126/science.280.5360.69.
14. Hou, Y., and Hou, X. (2021). Bioinspired nanofluidic iontronics. Science *373*, 628–629. https://doi.org/10.1126/science.abj0437.
15. Dekker, C. (2007). Solid-state nanopores. Nat. Nanotechnol. *2*, 209–215. https://doi.org/10.1038/nnano.2007.27.
16. Lei, D., Zhang, Z., and Jiang, L. (2024). Bioinspired 2D nanofluidic membranes for energy applications. Chem. Soc. Rev. *53*, 2300–2325. https://doi.org/10.1039/d3cs00382e.
17. Fan, R., Yue, M., Karnik, R., Majumdar, A., and Yang, P. (2005). Polarity Switching and Transient Responses in Single Nanotube Nanofluidic Transistors. Phys. Rev. Lett. *95*, 086607. https://doi.org/10.1103/PhysRevLett.95.086607.
18. Karnik, R., Fan, R., Yue, M., Li, D., Yang, P., and Majumdar, A. (2005). Electrostatic Control of Ions and Molecules in Nanofluidic Transistors. Nano Lett. *5*, 943–948. https://doi.org/10.1021/nl050493b.
19. Xue, Y., Xia, Y., Yang, S., Alsaid, Y., Fong, K.Y., Wang, Y., and Zhang, X. (2021). Atomic-scale ion transistor with ultrahigh diffusivity. Science *372*, 501–503. https://doi.org/10.1126/science.abb5144.
20. Wang, Y., Zhang, H., Kang, Y., Zhu, Y., Simon, G.P., and Wang, H. (2019). Voltage-Gated Ion Transport in Two-Dimensional Sub-1 nm Nanofluidic Channels. ACS Nano *13*, 11793–11799. https://doi.org/10.1021/acsnano.9b05758.

21. Fuest, M., Boone, C., Rangharajan, K.K., Conlisk, A.T., and Prakash, S. (2015). A Three-State Nanofluidic Field Effect Switch. Nano Lett. *15*, 2365–2371. https://doi.org/10.1021/nl5046236.

22. Jiang, Y., Liu, W., Wang, T., Wu, Y., Mei, T., Wang, L., Xu, G., Wang, Y., Liu, N., and Xiao, K. (2024). A nanofluidic chemoelectrical generator with enhanced energy harvesting by ion-electron Coulomb drag. Nat. Commun. *15*, 8582. https://doi.org/10.1038/s41467-024-52892-4.

23. Yang, J., Zhu, W., Zhang, X., Chen, F., and Jiang, L. (2019). Gated ion transport through layered graphene oxide membranes. New J. Chem. *43*, 7190–7193. https://doi.org/10.1039/C9NJ00460B.

24. Liu, W., Mei, T., Cao, Z., Li, C., Wu, Y., Wang, L., Xu, G., Chen, Y., Zhou, Y., Wang, S., et al. (2024). Bioinspired carbon nanotube–based nanofluidic ionic transistor with ultrahigh switching capabilities for logic circuits. Sci. Adv. *10*, eadj7867. https://doi.org/10.1126/sciadv.adj7867.

25. Wang, X., Zhang, H., Wei, G., Xing, J., Chen, S., and Quan, X. (2024). Co-mediation of voltage gating and ion charge in MXene membrane for controllable and selective monovalent cation separation. Sci. Adv. *10*, eado3998. https://doi.org/10.1126/sciadv.ado3998.

26. Vahidomahmmad, A., Rosen, J., and Gogotsi, Y. (2021). The world of two-dimensional carbides and nitrides (MXenes). Science *372*, eabf1581. https://doi.org/10.1126/science.abf1581.

27. Hantanasirisakul, K., and Gogotsi, Y. (2018). Electronic and Optical Properties of 2D Transition Metal Carbides and Nitrides (MXenes). Adv. Mater. *30*, 1804779. https://doi.org/10.1002/adma.201804779.

28. Ding, L., Li, L., Liu, Y., Wu, Y., Lu, Z., Deng, J., Wei, Y., Caro, J., and Wang, H. (2020). Effective ion sieving with $Ti_3C_2T_x$ MXene membranes for production of drinking water from seawater. Nat. Sustain. *3*, 296–302. https://doi.org/10.1038/s41893-020-0474-0.

29. Zhang, Y., Lei, L., Wang, J., Li, S., Liu, Y., Sun, Y., Liao, T., Chen, R., Wang, C., Wang, K., et al. (2025). Simultaneous voltage-gated control of ion and water transport in Zr4-$Ti_3C_2T_x$ nanochannel membranes. Nat. Commun. *16*, 8953. https://doi.org/10.1038/s41467-025-64007-8.

30. Kang, Y., Wang, Y., Zhang, H., Wang, Z., Zhang, X., and Wang, H. (2024). Functionalized 2D membranes for separations at the 1-nm scale. Chem. Soc. Rev. *53*, 7939–7959. https://doi.org/10.1039/d4cs00272e.

31. Gao, J., Feng, Y., Guo, W., and Jiang, L. (2017). Nanofluidics in two-dimensional layered materials: inspirations from nature. Chem. Soc. Rev. *46*, 5400–5424. https://doi.org/10.1039/c7cs00369b.

32. Cheng, C., Jiang, G., Simon, G.P., Liu, J.Z., and Li, D. (2018). Low-voltage electrostatic modulation of ion diffusion through layered graphene-based nanoporous membranes. Nat. Nanotechnol. *13*, 685–690. https://doi.org/10.1038/s41565-018-0181-4.

33. Yang, J., Hu, X., Kong, X., Jia, P., Ji, D., Quan, D., Wang, L., Wen, Q., Lu, D., Wu, J., et al. (2019). Photo-induced ultrafast active ion transport through graphene oxide membranes. Nat. Commun. *10*, 1171. https://doi.org/10.1038/s41467-019-09178-x.

34. Abraham, J., Vasu, K.S., Williams, C.D., Gopinadhan, K., Su, Y., Cherian, C.T., Dix, J., Prestat, E., Haigh, S.J., Grigorieva, I.V., et al. (2017). Tunable sieving of ions using graphene oxide membranes. Nat. Nanotechnol. *12*, 546–550. https://doi.org/10.1038/nnano.2017.21.

35. Goutham, S., Keerthi, A., Ismail, A., Bhardwaj, A., Jalali, H., You, Y., Li, Y., Hassani, N., Peng, H., Martins, M.V.S., et al. (2023). Beyond steric selectivity of ions using ångström-scale capillaries. Nat. Nanotechnol. *18*, 596–601. https://doi.org/10.1038/s41565-023-01337-y.

36. Esfandiar, A., Radha, B., Wang, F.C., Yang, Q., Hu, S., Garaj, S., Nair, R.R., Geim, A.K., and Gopinadhan, K. (2017). Size effect in ion transport through angstrom-scale slits. Science *358*, 511–513. https://doi.org/10.1126/science.aan5275.

37. Stein, D., Kruithof, M., and Dekker, C. (2004). Surface-Charge-Governed Ion Transport in Nanofluidic Channels. Phys. Rev. Lett. *93*, 035901. https://doi.org/10.1103/PhysRevLett.93.035901.

38. Kavokine, N., Netz, R.R., and Bocquet, L. (2021). Fluids at the Nanoscale: From Continuum to Subcontinuum Transport. Annu. Rev. Fluid Mech. *53*, 377–410. https://doi.org/10.1146/annurev-fluid-071320-095958.

39. Yang, J., Tu, B., Zhang, G., Liu, P., Hu, K., Wang, J., Yan, Z., Huang, Z., Fang, M., Hou, J., et al. (2022). Advancing osmotic power generation by covalent organic framework monolayer. Nat. Nanotechnol. *17*, 622–628. https://doi.org/10.1038/s41565-022-01110-7.

40. Xu, Y., Zhang, Z., Cui, Z., Luo, L., Lin, P., Xie, M., Zhang, Q., Sa, B., and Wen, C. (2024). Enhanced interfacial interactions and enriched active sites in self-assembly amino-functionalized bacterial cellulose/MXene composite for wastewater treatment. Chem. Eng. J. *488*, 151078. https://doi.org/10.1016/j.cej.2024.151078.

41. Hughes, C., Yeh, L.H., and Qian, S. (2013). Field Effect Modulation of Surface Charge Property and Electroosmotic Flow in a Nanochannel: Stern Layer Effect. J. Phys. Chem. C *117*, 9322–9331. https://doi.org/10.1021/jp402018u.

42. Liu, M., Zhang, H., Zhang, Z., Zhang, K., Chen, Z., Pan, L., and Zhou, J. (2024). Jujube-cake inspired lightweight and flexible MXene/liquid metal/bacterial cellulose electromagnetic interference shielding film with excellent Joule heating and thermal conductivity. Compos. Sci. Technol. *255*, 110722. https://doi.org/10.1016/j.compscitech.2024.110722.

43. Chen, L., Shi, G., Shen, J., Peng, B., Zhang, B., Wang, Y., Bian, F., Wang, J., Li, D., Qian, Z., et al. (2017). Ion sieving in graphene oxide membranes via cationic control of interlayer spacing. Nature *550*, 380–383. https://doi.org/10.1038/nature24044.

44. Zhou, X., Wang, Z., Epsztein, R., Zhan, C., Li, W., Fortner, J.D., Pham, T.A., Kim, J.H., and Elimelech, M. (2020). Intrapore energy barriers govern ion transport and selectivity of desalination membranes. Sci. Adv. *6*, eabd9045. https://doi.org/10.1126/sciadv.abd9045.

45. Wang, M., Xiong, Q., Yue, X., Yan, G., Han, Y., Lyu, Z., Li, Z., Sun, L., Hoenig, E., Xu, K., et al. (2025). Cooperative and inhibitory ion transport in functionalized angstrom-scale two-dimensional channels. Nat. Commun. *16*, 5854. https://doi.org/10.1038/s41467-025-61307-x.

46. Wang, G., Shao, L., and Zhang, S. (2025). Membrane-Ion Interactions Creating Dual-Nanoconfined Channels for Superior Mixed Ion Separations. Adv. Mater. *37*, 2414898. https://doi.org/10.1002/adma.202414898.

47. Shefer, I., Lopez, K., Straub, A.P., and Epsztein, R. (2022). Applying Transition-State Theory to Explore Transport and Selectivity in Salt-Rejecting Membranes: A Critical Review. Environ. Sci. Technol. *56*, 7467–7483. https://doi.org/10.1021/acs.est.2c00912.